

Optical Navigation System for Pin-Point Lunar Landing

V. Simard Bilodeau*, S. Clerc**, R. Draï***, J. de Lafontaine* ****

**Département de génie électrique et de génie informatique, Université de Sherbrooke, Sherbrooke, Canada (e-mail: vincent.simard.bilodeau@usherbrooke.ca).*

** *Thales Alenia Space, Cannes, France*

*** *European Space Research and Technology Centre, European Space Agency, Noordwijk, The Netherlands.*

**** *NGC Aerospace Ltd., Sherbrooke, Canada (e-mail: jean.delafontaine@ngcaerospace.com)*

Abstract: Major space agencies have an increasing interest in highly accurate (200 m) autonomous landing on the Moon. Inertial-only navigation is not compatible with this challenging requirement. The techniques currently investigated rely on vision-based navigation. A first approach consists in tracking features between sequences of images in order to measure the angular rate as well as the direction of the velocity vector of the spacecraft. A second approach aims at identifying image features using a geo-referenced on-board database to determine the attitude and the position of the spacecraft. However, existing algorithms are computationally prohibitive and have a limited robustness to varying illumination conditions and surface characteristics. This paper presents the development of an innovative autonomous vision-based navigation system addressing these problems. Numerical simulations have shown that this system is capable of estimating the position and velocity of the vehicle with an accuracy better than 100 m and 0.1 m/s respectively. This work is the result of a successful collaboration between the Université de Sherbrooke, NGC Aerospace Ltd., Thales Alenia Space and the European Space Agency. The proposed system has been selected as the main navigation algorithm in three major research and development projects sponsored by European Space Agency and the Canadian Space Agency.

Keywords: absolute optical navigation, relative optical navigation, state estimation, pin-point lunar landing, crater detection and matching, Harris corner tracking

INTRODUCTION

The interest of major space agencies for passive vision sensors in their mission design has been increasing over the years. These sensors are multipurpose, lightweight, space qualified and low cost. They offer an efficient solution to address the ever-increasing demands in navigation performance. The most widespread space application of a passive vision sensor is the star tracker (Wertz 1978). Star constellations in the camera images are recognized with the aim of retrieving the orientation of the spacecraft. Spacecraft rendezvous and docking (VBrNAV) (Di Sotto et al. 2005) is another example in which passive vision sensors are used. Distinctive and strategically arranged markers on the docking station are detected using image processing algorithms to retrieve the relative pose of the spacecraft with a high degree of accuracy. Moreover, interplanetary navigation systems (AUTONAV) (Bhaskaran et al. 2000) take the full advantage of cameras to provide the position of the spacecraft with respect to the target celestial bodies at long range. Finally, vision sensors are useful for planetary landing (DIMES, NPAL, ALHAT, VISINAV) (Cheng et al. 2004; Flandin et al. 2004; Brady et al. 2007; Mourikis et al. 2009) and small body sample and return (Kominato et al. 2006). In these applications, cameras open the way toward highly accurate positioning of the spacecraft by recognising visual features on the surface of the celestial body. All these vision-based navigation technologies have provided tremendous performance improvements of space navigation systems.

An important part of the research activities in passive vision sensing for space applications currently focuses on the navigation system for autonomous pin-point planetary landing and small-body sample and return. Without a Global Positioning System (GPS) or radio beacon, high-accuracy navigation around a non-terrestrial planet is a complex task. Most of the past and current navigation systems are based only on the accurate initialization of the states and on the integration of the Inertial Measurement Unit (IMU) measurements in order to obtain the translational and the angular position of the spacecraft (Trawny et al. 2007). This strategy can only track sudden motions of short duration, but their estimate diverges in time and typically leads to high landing error. This reality is mainly caused by the poorly-known gravity field of the celestial body and by the IMU measurement bias and noise. In order to improve navigation accuracy, many authors have proposed to fuse the IMU measurements with optical measurements using state estimators such as the Kalman filter.

A first vision-based navigation approach relies in feature tracking between sequences of images taken in real time during orbiting and/or landing operations. The features are pixels that have a high probability of being recognized between images taken from different camera locations. The information about the tracked features measures the angular rate and the direction of the velocity of the spacecraft. This technique, referred to as Terrain-Relative Navigation (TRRN), relies on relatively easy-to-implement, robust and well-developed image processing techniques. Although, this

technology has been demonstrated on space qualified hardware in DIMES (Cheng, Goguen et al. 2004) and NPAL (Flandin, Frapard et al. 2004), the gain in navigation accuracy remains limited since the spacecraft absolute position is not observed through the vision measurements. In fact, this technique normally helps maintaining an initial position accuracy, but the estimated position is not improved over time (it does not diverge as quickly compared to the inertial-only navigation approach).

A second vision-based navigation technique currently under investigation consists in identifying features and in mapping them into an on-board cartographic database indexed by an absolute coordinates system, thereby providing absolute position determination (Mourikis, Trawny et al. 2009). This technique, referred to as Terrain-Relative Absolute Navigation (TRAN), relies on complex Image Processing Software (IPS) that are not compatible with flight computers and have an obvious lack of robustness.

To be usable in future pinpoint landing missions, vision-based navigation technology must meet the following well-established requirements:

1. High accuracy: The navigation system shall provide absolute position and surface-relative velocity knowledge within respectively tens of meters (100 m) and tens of millimetres per second (10 cm/s) at touchdown.
2. Autonomy: The navigation system shall operate without intervention from the ground.
3. Compatibility with flight computers: Flight computers typically have limited computing power and require highly optimized and computer-efficient algorithms.
4. Robustness: The navigation system shall be able to work in a wide variety of environments which means varying light conditions, varying atmospheric conditions, different spacecraft altitudes, different viewing angles and with a wide range of surface topography, albedo and texture.

The main objective of the paper is to present the development of an accurate, robust, autonomous and computational efficient vision-based navigation algorithm that provides absolute position and surface-relative velocity during the proximity operation of the lunar landing mission using a combined approach of TRRN and TRAN. This work is the result of a joint research and development endeavour sponsored by the Université de Sherbrooke, NGC Aerospace Ltd., the European Space Agency and Thales Alenia Space.

This paper first describes the space mission for which the system has been developed. It is followed by an overview of the navigation system. The proposed image processing and estimation algorithms are then described. Finally, numerical simulation experiments are presented in order to demonstrate the performance of the system.

MISSION DEFINITION

1.1. Mission Timeline

There are several missions that would benefit from TRAN and TRRN. However, this work focuses on lunar landing mission. This mission aims at delivering a payload to a precise location on the surface of the Moon or at reaching a

specific site with a high scientific interest. The mission timeline is based on the Next Lunar Lander (NLL) study (Pradier et al. 2011). The targeted landing site is located at the Malapert peak. The descent trajectory is decomposed into the three phases shown in the following figure:

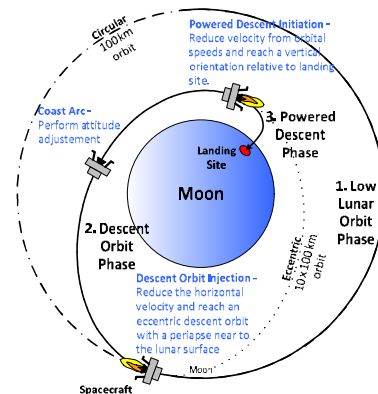


Fig. 1: Phases of the Moon-Landing Mission

The Low Lunar Orbit (LLO) phase begins when the vehicle is in a circular orbit at an altitude of 100 km. The LLO phase ends when the Descent Orbit Injection (DOI) is performed in order to bring the vehicle into the Descent Orbit (DO). More precisely, the DOI reduces the horizontal velocity of the spacecraft to reach an eccentric descent orbit with a periapee close to the lunar surface. The Power Descent Initialization (PDI) takes place around an altitude of 10 km. During the Powered Descent (PD), the velocity of the spacecraft is reduced from orbital speed (~ 1.7 km/s) to a velocity safe for landing (1 m/s).

The PD phase has four parts. At the beginning, the spacecraft follows a predefined optimal trajectory computed using numerical optimisation tools. The optimization problem is formulated following the Pontryagin's maximum/minimum principle (Lewis 2006). At 80 km of downrange, the Powered Explicite Guidance (PEG) algorithm is enabled (Springmann 2006). This algorithm has been originally developed for the space shuttle. It aims at computing the thrust direction and magnitude to reach a desired terminal position \mathbf{r}_d and velocity \mathbf{v}_d in a minimum time using a computationally-efficient iterative algorithm. When the spacecraft reaches an altitude of about 100 m, the Gravity Turn (GT) segment is engaged. This guidance law lines up the engines of the vehicle to fire in the opposite direction of its current surface-relative velocity vector. At 10 m of altitude or when the spacecraft reaches a vertical velocity of 1 m/s the Terminal Descent (TD) phase starts. During this phase, the spacecraft descends at a constant velocity toward the ground. Finally, when the landing legs touch the ground, the engines are cut off.

1.2. Lightning conditions

The mission takes place with illumination conditions that are challenging for optical-based navigation. The descent orbit of the spacecraft is assumed to be at 45 degrees of the terminator as shown in Fig. 2 below:

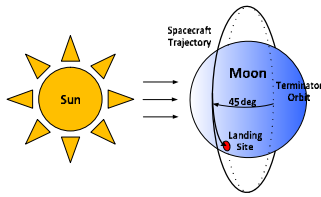


Fig. 2: Landing Orbit and Assumption about the Sun Position

The terminator is the line which separates the illuminated day side and the dark night side of the Moon. During landing the light elevation vary from 45 to 2.5 deg.

1.3. Sensor Suite

The navigation sensor suite comprises: an Inertial Measurement Unit (IMU), a star tracker, an altimeter and a camera. The configuration of the sensors on the vehicle is shown in the following figure:

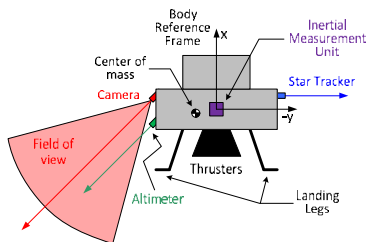


Fig. 3: Sensor Configurations

The IMU is used during the entire mission. The star tracker is enabled only when the main engines are cut off, *i.e.* during the DO. The perturbations induced by thrusters can interfere with the operation of the star tracker and yield to erroneous spacecraft attitude measurements. The altimeter is enabled as soon as the spacecraft altitude is compatible with its maximum operating range of 3 km. This happens at an altitude of 2 km. The altimeter operation is stopped when the terminal descent starts. At this point, the interaction of the thruster plumes with the ground raises dust which might affect its operation. The absolute optical navigation is enabled at an altitude of 50 km. There are many reasons why enabling the absolute navigation earlier is not useful. First, at higher altitude, the low resolution of the image makes the absolute optical measurements so inaccurate that they do not provide significant improvements to the spacecraft position and attitude estimation. Second, accurate spacecraft position knowledge is not required since the translational states of the spacecraft are left uncontrolled during the DO phase. Third, the use of optical absolute navigation early in the descent would require a larger on-board database. However, it is critical to start the absolute navigation before the braking burn. The powered descent phase must be initiated at the right moment during the descent in order to fulfil the challenging landing accuracy requirements using a minimum amount of fuel. The absolute optical navigation is disabled at an altitude of 1.5 km. At lower altitude, the absolute navigation would require an on-board geo-referenced feature database with a resolution higher than that of the currently available lunar surface imagery. The optical relative navigation is started only at an altitude of 25 km. In other to get a relatively accurate velocity estimation of the spacecraft from the relative optical measurements, the resolution of the

image must be sufficiently good. In addition, the velocity estimates are more accurate if the altitude estimation error is lower. Consequently, it is more adequate to let the navigation filter converges using the absolute optical measurements before starting the optical relative navigation.

NAVIGATION SYSTEM OVERVIEW

The proposed navigation system used both TRRN and TRAN technology. It is shown in the following figure:

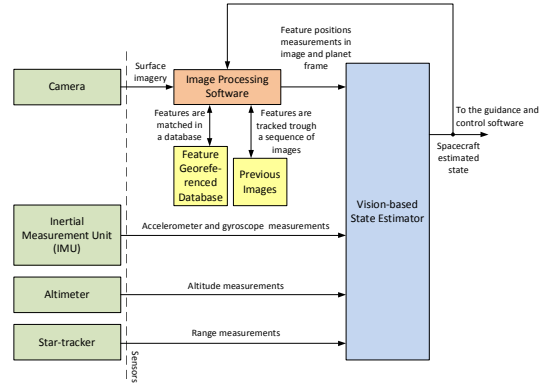


Fig. 4: Navigation System Overview

For the TRRN, the IPS tracks several features into successive image frames. It provides the normalized image coordinates of the features. For TRAN, the IPS detects and matches the features into a geo-referenced database. Consequently, the feature information is augmented by their surface position. The information extracted by the image processing and the measurements from other sensors are fed into an Extended Kalman Filter (EKF) to estimate the spacecraft states (position, velocity, and attitude).

IMAGE PROCESSING

1.4. Crater Detection and Matching

The presence of relatively well-shaped crater impacts covering the entire surface makes the Crater Detection and Matching Algorithm (CDMA) an attractive solution for future autonomous robotic lunar landing missions.

The crater detection is achieved by pairing shadowed and illuminated objects of the image having a similar size and a relative orientation consistent with the direction of the light. The proposed algorithm is able to detect craters close from each other as well as eroded craters of various size. It is also robust to a wide range of illumination conditions and terrain characteristics. The details of this algorithm are presented in Fig. 5. It has eight steps:

1. A rough estimation of the Sun direction in the image is computed using the estimated states of the spacecraft (position and orientation) and the Moon and Sun ephemerides.
2. The image is filtered using a smoothing filter to reduce image noise and the high-frequency texture induces by the terrain relief (not useful information for crater detection). The image is also equalized in order to exploit the full range of intensity values.

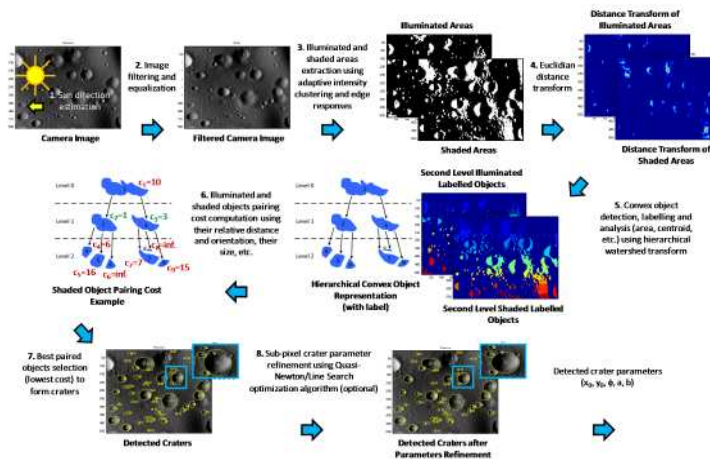


Fig. 5: Crater Detection

3. Illuminated and shaded objects are extracted from the images using adaptive intensity clustering and the image edge response. The result of this operation is two binary images describing the illuminated and shaded objects in the image.
 4. The distance transform is then applied on the binary images so the intensity of each object pixel becomes proportional to its distance from the closest background pixel.
 5. A hierarchical watershed transform is performed in order to extract the convex illuminated and shaded objects (potentially parts of craters). Each convex object is labelled and characterized (area, centroid, principal axes). The result of this step is a hierarchical representation of each illuminated and shaded object referred as object trees. Each level of the hierarchy represents a higher level of object segmentation.
 6. All combinations of illuminated and shaded convex object pairs are compared against a simple mathematical model of a crater. This model characterizes for instance the relative size of objects, their distance versus their size, and their relative orientation with respect to the Sun direction. Each illuminated/shaded object pair is assigned to a cost proportional to its degree of dissimilarity to the crater mathematical model.
 7. In order to keep only the best candidate craters and remove multiple pairings of same convex object, a dynamic optimization algorithm exploiting the quality of the pairs is used. This process starts by identifying the object pair with the lowest cost value (highest quality). The trees of these objects are then used to identify their parent and their children in order to ungroup them. Consequently, it is no longer possible for them to form craters. In addition, other pairs composed of one of the objects (which have by definition a higher cost) are also ungrouped. Therefore, the same object cannot belong to more than one crater. This scheme is repeated with the pair having the second lowest cost among all remaining pairs and so on until that all pairs are processed.
 8. The parameters of the ellipse characterizing each detected crater are computed. In order to do so, the smallest ellipse enclosing all the pixels of the crater objects is determined.
- The crater matching algorithm uses the parameters of the detected craters to locate them into a geo-referenced database. The proposed algorithm is based on a stochastic approach robust to false detection, missed detection and/or depleted database. It also provides very few false matches (see next sections). The proposed algorithm exploits the logical consistency between matches (a given detected crater cannot be matched to more than one database crater and vice versa) as well as the geometric consistency of a match (detected and database craters of the matches are related through a camera projection model). The algorithm is summarized below:
1. A set of logically consistent tentative matches (2 or more) is picked randomly. The probability of selecting a match is proportional to the degree of geometrical consistency with the current estimate of the spacecraft attitude and position.
 2. The camera position is estimated from the set drawn in step 1 using a least square fit approach.
 3. The number of matches geometrically consistent with this computed camera position is determined.
 4. The matches with incompatible radius are removed.
 5. The steps 2 to 4 are repeated using the matches found in step 4.
 6. If more than 50% of the detected craters are matched, stop the algorithm.
 7. If the maximum number of iterations is not exceeded, restart at step 1. Otherwise, no match has been found.

1.5. Harris Corner Tracking

Harris corners can be detected in image with a minimum among of texture. They can be easily tracked in an image sequence using the approach illustrated in Fig. 6 and summarized as follows:

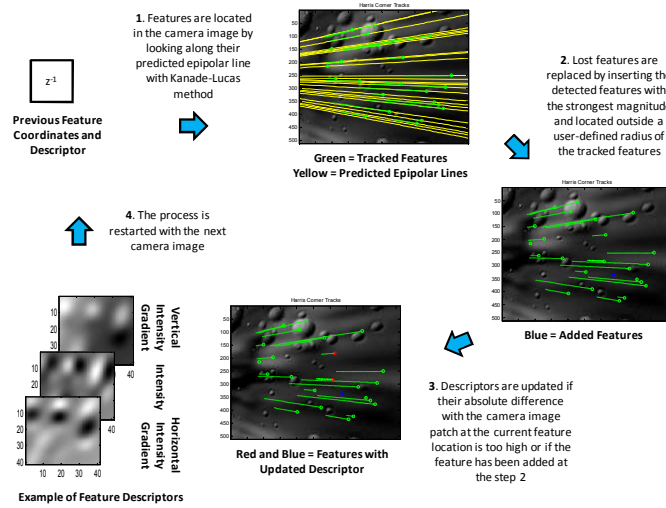


Fig. 6: Harris Corner Tracking

1. The algorithm searches for each feature in the current image along the predicted epipolar line with the Kanade-Lucas (KL) differential method (Robinson 2004).
2. The lost tracks are then replaced by the strongest corners of the current image located outside a user-defined radius of the tracked features.
3. The descriptor of each feature is updated if their sum of squared difference with the current image is too high or if the corner has been newly added in step 2. The feature descriptor corresponds to the intensity as well as the vertical and horizontal intensity gradient of the pixels in the corner neighbourhood (this descriptor is required in the step 1).
4. The process is then restarted when a new image is available using the updated feature coordinates and descriptors.

VISION-BASED STATE ESTIMATOR

The proposed state estimation is based on the multiplicative version of the Extended Kalman Filter (EKF) (Chodas 1982). This formulation is able to deal with quaternion in its state vector. This algorithm is well known and will be not reported in this paper. The major challenges faced in the design of a robust and accurate filter are the selection of the state vector and the definition of the mathematical models describing the state evolution and the measurements as function of states. It is noted that the measurement equations can also be formulated as constraints between the states and the measurements. These models must also include the various noise sources of the system (assumed zero-mean Gaussian random signal). The covariance of the noise signals defines the weight of the state propagation and of each measurement update in the estimation. Following the Kalman filter theory, the state estimator also keeps track of the current state estimation covariance. This information can be used as a quality indicator.

1.6. State Vector

The proposed state vector is given by:

$$\mathbf{x} = [\mathbf{q}_{BP} \quad \boldsymbol{\omega}_{BI}^B \quad \mathbf{b}_{\omega}^B \quad \mathbf{p}_{Sc}^P \quad \mathbf{v}_{Sc}^P \quad \mathbf{a}_{Sc}^B \quad \mathbf{b}_a^B]^T \quad (1)$$

where \mathbf{q}_{BP} is a quaternion describing the rotation from the planet fixed frame \mathfrak{I}^P to the spacecraft body frame \mathfrak{I}^B , $\boldsymbol{\omega}_{BP}^B$ is the angular velocity of the spacecraft with respect to \mathfrak{I}^P and expressed in \mathfrak{I}^B , \mathbf{a}_{Sc}^B is the acceleration of the spacecraft excluding the gravity in \mathfrak{I}^B , \mathbf{v}_{Sc}^P and \mathbf{p}_{Sc}^P are the spacecraft velocity and position expressed in \mathfrak{I}^P , \mathbf{b}_{ω}^B and \mathbf{b}_a^B are the gyroscope and the accelerometer bias in \mathfrak{I}^B .

As it will be shown in the next section, the relative optical measurements are used to enforce constraints between two past spacecraft poses (attitude quaternion and position). It will be also explained that the optical measurements (especially the absolute ones) are available several seconds after the image acquisition due to the processing time. Consequently, the measurements are not consistent with the current states of the spacecraft. In order to deal with these facts, the state vector is augmented with a history of past spacecraft poses (position and quaternion):

$$\mathbf{x}_a = [\mathbf{x} \quad \dots \quad \mathbf{x}_{h,i} \quad \dots]^T \quad (2)$$

where $\mathbf{x}_{h,i} = [\mathbf{q}_{BP,h,i} \quad \mathbf{p}_{Sc,h,i}^P]$. Each time an image is triggered, the oldest pose from the history is replaced with the current vehicle pose and the covariance is updated accordingly. These poses are fixed in time and only their cross-covariance with the current spacecraft pose evolves. Consequently, an update of the past poses also impacts the estimation of the current states.

1.7. Spacecraft Model

The spacecraft dynamic model is given in the following equations:

$$\dot{\mathbf{q}}_{BP} = \frac{1}{2} \boldsymbol{\Omega} (\boldsymbol{\omega}_{BI}^B - \mathbf{C}(\mathbf{q}_{BP}) \boldsymbol{\omega}_{PI}^P) \mathbf{q}_{BP} \quad (3)$$

$$\dot{\boldsymbol{\omega}}_{Sc}^B = \boldsymbol{\eta}_{\alpha}^B \quad (4)$$

$$\dot{\mathbf{b}}_{\omega}^B = \boldsymbol{\eta}_{b_{\omega}}^B \quad (5)$$

$$\dot{\mathbf{v}}_{Sc}^P = \mathbf{g}^P + \mathbf{C}(\mathbf{q}_{BP})^T \mathbf{a}_{Sc}^B - 2(\boldsymbol{\omega}_{PI}^P)^\times \mathbf{v}_{Sc}^P - (\boldsymbol{\omega}_{PI}^P)^\times (\boldsymbol{\omega}_{PI}^P)^\times \mathbf{p}_{Sc}^P + \boldsymbol{\eta}_g^P \quad (6)$$

$$\dot{\mathbf{a}}_{Sc}^B = \boldsymbol{\eta}_a^B \quad (7)$$

$$\dot{\mathbf{b}}_a^B = \boldsymbol{\eta}_{b_a}^B \quad (8)$$

where $\mathbf{C}(\mathbf{q})$ is the cosine direction matrix corresponding to \mathbf{q} , $\boldsymbol{\omega}^\times$ is the skew-symmetric matrix of the vector $\boldsymbol{\omega}$, $\boldsymbol{\omega}_{PI}^P$ is the

angular velocity of the Moon with respect to the inertial frame and expressed in its reference frame, $\boldsymbol{\eta}_g^p$ represents the gravity field modelling error, $\boldsymbol{\Omega}(\boldsymbol{\omega})$ and \boldsymbol{g}^p are respectively defined by:

$$\boldsymbol{\Omega}(\boldsymbol{\omega}) = \begin{bmatrix} \mathbf{0} & -\boldsymbol{\omega}^T \\ \boldsymbol{\omega} & -\boldsymbol{\omega}^\times \end{bmatrix} \quad (9)$$

$$\boldsymbol{g}^p = -\frac{\mu}{\|\boldsymbol{p}_{Sc}^p\|^3} \boldsymbol{p}_{Sc}^p \quad (10)$$

1.8. Gyroscope and Acceleration Measurement Model

The gyroscope and acceleration measurement models are respectively shown below:

$$\tilde{\boldsymbol{\omega}}_{Bl}^B = \boldsymbol{\omega}_{BP}^B + \mathbf{C}(\boldsymbol{q}_{BP}) \boldsymbol{\omega}_{Pl}^p + \boldsymbol{b}_\omega^B + \boldsymbol{\eta}_\omega^B \quad (11)$$

$$\tilde{\boldsymbol{a}}_{Sc}^B = \boldsymbol{a}_{Sc}^B + \boldsymbol{b}_a^B + \boldsymbol{\eta}_a^B \quad (12)$$

where $\boldsymbol{\omega}_{Pl}^p$ is the angular velocity of the planet with respect to \mathfrak{S}^I expressed in \mathfrak{S}^p , $\boldsymbol{\eta}_\omega^B$ and $\boldsymbol{\eta}_a^B$ are the gyroscope and the accelerometer noise.

1.9. Optical-Absolute Measurement Model

The optical absolute measurements are processed using the pin-hole projection model based on the crater line-of-sight:

$$\tilde{\boldsymbol{u}}_i = \begin{bmatrix} 1 & 0 & 0 \\ 0 & 1 & 0 \\ 0 & 0 & 1 \end{bmatrix} \boldsymbol{p}_{Feai}^C + \boldsymbol{\eta}_{Abs,i} \quad (13)$$

where $\boldsymbol{\eta}_{Abs,i}$ is the crater detection measurement noise, \boldsymbol{p}_{Feai}^C is the position of feature i in the camera frame $\tilde{\mathfrak{S}}^C$:

$$\boldsymbol{p}_{Feai}^C = \mathbf{C}(\boldsymbol{q}_{CB}) [\mathbf{C}(\boldsymbol{q}_{BP,h,i}) (\tilde{\boldsymbol{p}}_{Feai}^p + \boldsymbol{\eta}_{Map} - \boldsymbol{p}_{Sc,h,i}^p) - \boldsymbol{p}_{Cam}^B] \quad (14)$$

\boldsymbol{p}_{Feai}^p is the crater surface position, \boldsymbol{p}_{Cam}^B and \boldsymbol{q}_{CB} are the attitude quaternion and the position of the camera in \mathfrak{S}^B , $\boldsymbol{\eta}_{Map}$ is the map-tie error (error in the on-board crater database).

1.10. Optical-Relative Measurement Model

The optical relative measurements are treated using the epipolar constraint defined between two different views of the same feature (taken at different time):

$$0 = \begin{bmatrix} \tilde{\boldsymbol{u}}_{i,j} + \boldsymbol{\eta}_{Rel,i,j} \\ 1 \end{bmatrix}^T \boldsymbol{R} \boldsymbol{T}^\times \begin{bmatrix} \tilde{\boldsymbol{u}}_{i,l} + \boldsymbol{\eta}_{Rel,i,j} \\ 1 \end{bmatrix} \quad (15)$$

where \boldsymbol{R} is the director cosine matrix that describes the rotation from the view l to the view j , \boldsymbol{T}^\times corresponds to the skew-symmetric matrix of the translation vector between the two views:

$$\boldsymbol{R} = \mathbf{C}(\boldsymbol{q}_{CB}) \mathbf{C}(\boldsymbol{q}_{BP,h,j}) (\mathbf{C}(\boldsymbol{q}_{CB}) \mathbf{C}(\boldsymbol{q}_{BP,h,l}))^T \quad (16)$$

$$\boldsymbol{T} = \mathbf{C}(\boldsymbol{q}_{CB}) \mathbf{C}(\boldsymbol{q}_{BP,h,l}) (\boldsymbol{p}_{Sc,h,j}^p + \mathbf{C}^T(\boldsymbol{q}_{BP,h,j}) \boldsymbol{p}_{Cam}^B - (\boldsymbol{p}_{Sc,h,l}^p + \mathbf{C}^T(\boldsymbol{q}_{BP,h,l}) \boldsymbol{p}_{Cam}^B)) \quad (17)$$

1.11. Altimeter Measurement Model

The altimeter measurements are fused using the following constraint:

$$0 = (\boldsymbol{n}_{Srf}^p)^T \boldsymbol{p}_{Ptd}^p + d_{Srf} \quad (18)$$

where \boldsymbol{n}_{Srf}^p and d_{Srf} are the parameter of the surface mean plane. The surface mean plane can be predetermined prior the mission if the trajectory is such that the altimeter is pointed toward the landing during the descent or it can be recomputed in the real-time using an on-board Digital Elevation Map (DEM). The point \boldsymbol{p}_{Ptd}^p of Eq. (18) is defined as:

$$\boldsymbol{p}_{Ptd}^p = \mathbf{C}^T(\boldsymbol{q}_{BP}(k - d_{Alt})) \boldsymbol{p}_{Ptd}^A + \boldsymbol{p}_{Sc}^p(k - d_{Alt}) \quad (19)$$

where d_{Alt} is the altimeter measurement delay and \boldsymbol{p}_{Ptd}^A is given by:

$$\boldsymbol{p}_{Ptd}^A = \mathbf{C}(\boldsymbol{q}_{AB})^T [0 \ 0 \ 1]^T (\tilde{r}(k - d_{Alt}) + \eta_{Alt}) + \boldsymbol{p}_{Alt}^B \quad (20)$$

The vectors $\boldsymbol{p}_{Sc}^p(k - d)$ and $\boldsymbol{q}_{BP}(k - d)$ correspond to the back-propagated position and attitude of the spacecraft at the time of the measurement:

$$\boldsymbol{p}_{Sc}^p(k - d) = \boldsymbol{p}_{Sc}^p - \boldsymbol{v}_{Sc}^p t_d + \frac{1}{2} \left(\begin{array}{c} \mathbf{C}(\boldsymbol{q}_{BP})^T \boldsymbol{a}_{Sc}^B - \frac{\mu}{\|\boldsymbol{p}_{Sc}^p\|^3} \boldsymbol{p}_{Sc}^p \\ -2(\boldsymbol{\omega}_{Pl}^p)^\times \boldsymbol{v}_{Sc}^p - (\boldsymbol{\omega}_{Pl}^p)^\times (\boldsymbol{\omega}_{Pl}^p)^\times \boldsymbol{p}_{Sc}^p \end{array} \right) d^2 \quad (21)$$

$$\boldsymbol{q}_{BP}(k - d) = \cos\left(\frac{d}{2} \|\boldsymbol{\omega}_{BP}^B\|\right) \boldsymbol{q}_{BP} - \frac{1}{\|\boldsymbol{\omega}_{BP}^B\|} \sin\left(\frac{d}{2} \|\boldsymbol{\omega}_{BP}^B\|\right) \begin{bmatrix} -\boldsymbol{q}_{BP,*}^T \\ \boldsymbol{q}_{BP,*}^\times + \boldsymbol{q}_{BP,0} \boldsymbol{I}_{3 \times 3} \end{bmatrix} \boldsymbol{\omega}_{BP}^B \quad (22)$$

This delay-recovery method is less elegant than the one used for optical measurement fusion, but it is more computationally efficient and accurate enough when the delay is small (a few navigation cycles).

1.12. Star-Tracker Measurement Model

The star-tracker measurement equation is given by the following constraint:

$$\mathbf{0}_{3 \times 1} = [\mathbf{0}_{3 \times 1} \ \boldsymbol{I}_{3 \times 3}] \left(\begin{bmatrix} \mathbf{1} \\ 0.5 \boldsymbol{\eta}_{Str} \end{bmatrix} \otimes \boldsymbol{q}_{SB} \otimes \boldsymbol{q}_{BP}(k - d_{Str}) \otimes \boldsymbol{q}_{Pl} \otimes (\tilde{\boldsymbol{q}}_{Sl}(k - d_{Str}))^{-1} \right) \quad (23)$$

where \otimes is the quaternion product, $\tilde{\boldsymbol{q}}_{Sl}$ is the measured quaternion from \mathfrak{S}^I to the star-tracker frame, $\boldsymbol{\eta}_{Str}$ is the star-tracker measurement noise, \boldsymbol{q}_{SB} is the orientation of the star-tracker frame in \mathfrak{S}^B , \boldsymbol{q}_{Pl} is the planet attitude quaternion in \mathfrak{S}^I (computed from the on-board time), d_{Str} is the star-tracker measurement delay. The back-propagated spacecraft quaternion $\boldsymbol{q}_{BP}(k - d_{Str})$ has been defined in the previous paragraph.

SIMULATION TESTING

1.13. Crater Detection and Matching Robustness Analysis

The crater detection and matching is a critical part of the navigation system. Several analyses have been done to demonstrate its robustness. Those analyses use more than 4000 synthetic images generated with PANGU (Parkes et al. 2004). The first analysis demonstrates that the algorithm is robust to translational motion blur of more than 4 pixels (which is severe considering that the blur is lower than one pixel during the descent):

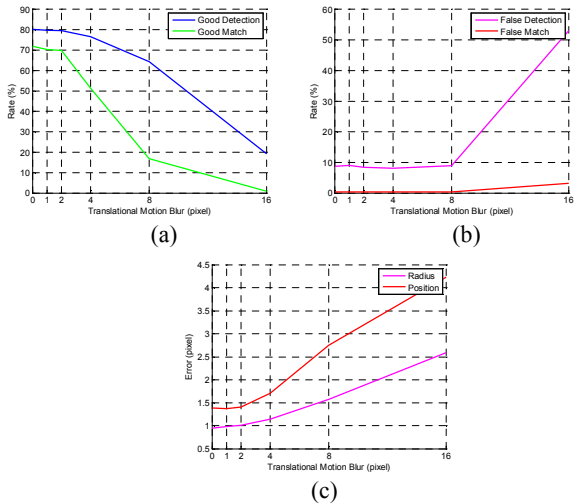


Fig. 7: Crater Detection Performance Versus Translational Motion Blur (a) detection and matching rate, (b) false detection and false match rate, (c) crater radius and position accuracy

The second analysis shows that image Signal to Noise Ratio (SNR) has to be only 20 to get good crater detection and matching performances (lighting condition analysis shown that typical SNR of the images gathered during the descent is 50):

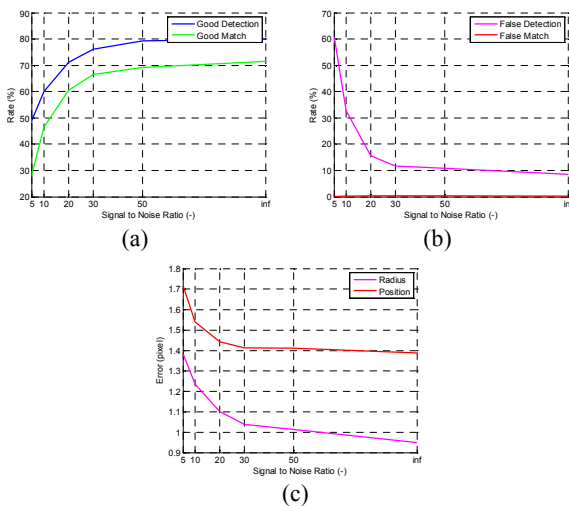


Fig. 8: Image Processing Performance Versus Image Noise (a) detection and matching rate, (b) false detection and false match rate, (c) crater radius and position accuracy

The third and fourth analyses demonstrate that the crater detection and matching algorithm works for a wide range of realistic Sun elevations angles and viewing angles:

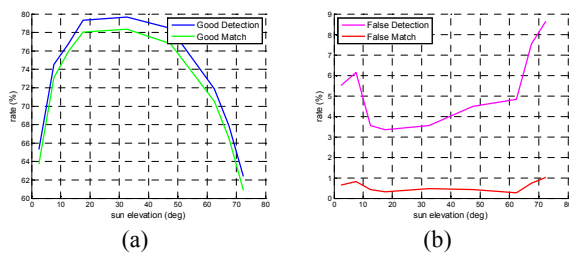


Fig. 9: Image Processing Performance Versus Viewing Angle (a) detection and matching rate, (b) false detection and false match rate, (c) crater radius and position accuracy

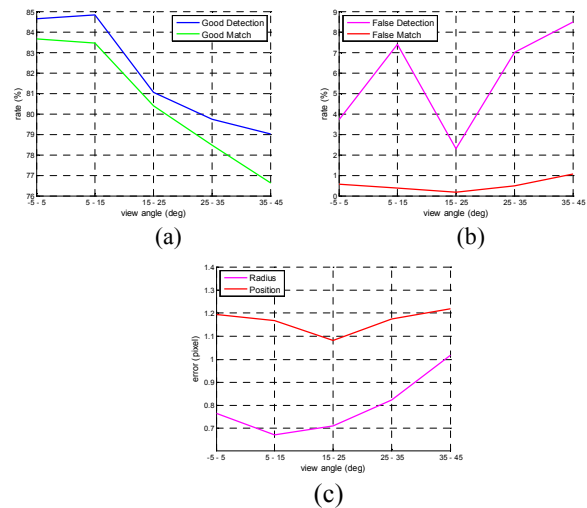


Fig. 10: Image Processing Performance Versus Light Elevation (a) detection and matching rate, (b) false detection and false match rate, (c) crater radius and position accuracy

1.14. High Fidelity, End-to-End Closed-Loop Simulation

The navigation system has also been validated using high fidelity, closed-loop and end-to-end simulations using MATLAB/SIMULINK. It is noted that only a few papers have published results of end-to-end lunar landing simulations with image processing in the loop. The real-world simulator includes the following components:

- The camera images are generated during the simulation based on the true states of the vehicle using PANGU.
- The distribution of the craters and their size are based on (Smith et al. 1982).
- The topography of the surface is defined using the Kaguya mission flight data (Araki et al. 2009).
- The map-tie error of the crater on-board database has been established so it is representative of the currently available positioning information of the lunar craters (50 m).
- The camera lens and intrinsic parameter calibration errors are modelled.
- The lighting conditions are representative of the mission scenario.
- The characteristics of the Charged Coupled Device (CCD) are based on the Atmel TH7888.
- The IMU model is based on the Honeywell YG9666N characteristics.
- The star-tracker model is based on the ASTRO-APS sold by Jenaoptronik.

- The altimeter model corresponds to the Doppler radar designed for the EXOMARS mission.
- The propulsion system as well as the fuel slosh is fully modelled.
- The gravity field is modelled using LP165 (Konopliv et al. 2000).

The on-board software includes:

- The crater detection and matching as well as the Harris corner tracking coded in C language.
- The state estimator implemented in SIMULINK.
- The guidance and control algorithm based on the design described in (Hamel et al. 2012) and implemented in SIMULINK.

Typical attitude, position and velocity estimation accuracy is shown in the following figure:

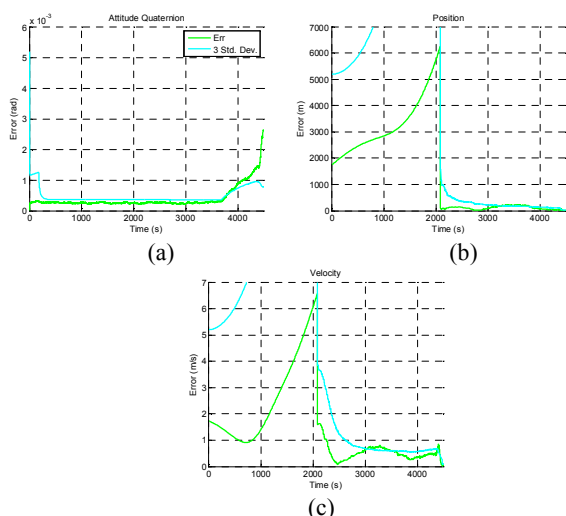


Fig. 11: Navigation Error Versus Time, (a) attitude, (b) position, (c) velocity

The estimation errors are reported by phase of the mission in the following table:

Tab. 1: Navigation Errors

Mission Phase	Position (m)	Velocity (m/s)	Attitude (rad)
Before the enabling of the optical navigation	6.1×10^3	6.4	2.4×10^{-4}
PDI	230	0.60	2.8×10^{-4}
TD	8.6	0.033	0.0026

One could notice a dramatic improvement of the position estimation accuracy when the crater detection and matching is enabled. The position and the velocity estimation accuracy at TD are respectively of the order of 10 m and 5 cm/s which fulfil with a comfortable margin the mission requirements.

CONCLUSIONS

This paper has presented an innovative optical navigation system for lunar pin-point landing. Its performance has also been demonstrated through high-fidelity end-to-end simulations. The attitude, position and velocity estimation errors are lower than 0.15 deg, 10 m and 0.05 m/s respectively. For future work, the image processing will be implemented on flight-like computer.

ACKNOWLEDGEMENTS

This work was financially supported by the European Space Agency under the NPI program and by NGC Aerospace Ltd (Canada).

REFERENCES

Araki, H., S. Tazawa, et al. (2009). Lunar Global Shape and Polar Topography Derived from Kaguya-LALT Laser Altimetry. *Science*, 323 (5916), 897-900.

Bhaskaran, R., J. S. Desai, et al. (2000). Using Autonomous Navigation for Interplanetary Missions: Mission Operations with Deep Space 1 Autonav. *Proceedings of the 6th Space Operations Conference*, Toulouse, France.

Brady, T. and J. Schwartz (2007). ALHAT System Architecture and Operation Concept. *Proceedings of the IEEE Aerospace Conference*, Big Sky, Montana.

Cheng, Y., J. Goguen, et al. (2004). The Mars Exploration Rovers Descent Image Motion Estimation System. *IEEE Intelligent Systems*, 19 (3).

Chodas, P. W. (1982). Combined Satellite Attitude and Orbit Determination with Dynamic Coupling. *Proceedings Astrodynamics Conference*, San Diego, California.

Di Sotto, E., L. F. Penin, et al. (2005). Design of Guidance and Control Algorithms for a Vision Based Navigation Rendezvous Mission on Mars Orbit. *Proceedings of the 56th International Astronautical Congress of the International Astronautical Federation*, Fukuoka, Japan.

Flandin, G., B. Frapard, et al. (2004). Design and Validation of a Vision Based Navigation Camera for Space Exploration. *Proceedings of the 14e Congrès Reconnaissance des Formes et Intelligence Artificielle*, Paris, France.

Hamel, J.-F., D. Beaudette, et al. (2012). GNC Design & Validation for Precision Landing at the Moon and Mars. *Proceedings of the 35th Annual ASSS Guidance and Control Conference*, Breckenridge, Colorado.

Kominato, T., M. Matsuoka, et al. (2006). Optical Hybrid Navigation and Station Keeping around Itokawa. *Proceedings of the AIAA/ASIS Astrodynamics Specialist Conference and Exhibit*, Keystone, Colorado.

Konopliv, A. S., S. W. Asmar, et al. (2000). *Recent Gravity Models as a Result of the Lunar Prospector Mission*. Jet Propulsion Laboratory, Pasadena.

Lewis, A. D. (2006). *The Maximum Principle of Pontryagin in Control and in Optimal Control*. Queen's University, Kingston.

Mourikis, A. I., N. Trawny, et al. (2009). Vision-Aided Inertial Navigation for Spacecraft Entry, Descent, and Landing. *IEEE Transactions on Robotics*, 25 (2), 264-280.

Parkes, S. M., I. Martin, et al. (2004). Planet Surface Simulation with PANGU. *Proceedings of the 8th International Conference on Space Operations*, Montreal, Canada.

Pradier, A., B. Gardini, et al. (2011). The ESA Lunar Lander Mission. *Proceedings of the 8th International Planetary Probe Workshop*, Portsmouth, Virginia.

Robinson, D. (2004). *Estimation Theoretic Analysis of Motion in Image Sequences*. University of California, Santa Cruz.

Smith, R. E. and G. S. West (1982). *Space and Planetary Environment Criteria Guidelines for Use in Space Vehicle Development*. Marshall Space Flight Center, Huntsville.

Springmann, P. N. (2006). *Lunar Descent Using Sequential Engine Shutdown*. Massachusetts Institute of Technology, Cambridge.

Trawny, N., A. I. Mourikis, et al. (2007). Vision-Aided Inertial Navigation for Pin-Point Landing using Observations of Mapped Landmarks. *Journal of Field Robotics*, 24 (5), 357-378.

Wertz, J. R. (1978). *Spacecraft Attitude Determination and Control*. Kluwer Academic Publishers, Dordrecht.